processes

MDPI

*Article*

# Development of a Shear-Responsive Gel for Lost Circulation Control Tailored to Enhance Drilling Rate of Penetration

**Shoushuai Huang [1], Zhigang Zhang [1,*], Jian Mao [1], Bin Li [1], Ruigang Yuan [1], Zhaomin Jiang [1] and Shubin Liu [2]**

[1] Drilling Measurement and Control Research Center, Directional Well Technical Service Company of XDEC, Urumqi 830063, China; huangshoushuai@163.com (S.H.); maojianxj@cnpc.com.cn (J.M.); jcmxj@cnpc.com.cn (Z.J.)
[2] School of Petroleum Engineering, China University of Petroleum (East China), Qingdao 266580, China; q20240047@upc.edu.cn
* Correspondence: zhangzg0524@163.com

## Abstract

Lost circulation of wellbore fluids within fissured zones constitutes a primary factor contributing to increased non-productive time (NPT) and restricted rate of penetration (ROP). Conventional gel-based lost circulation materials (LCMs) inherently suffer from a trade-off between pumpability and in situ fracture retention, and they lack a design methodology quantitatively correlated with drilling engineering parameters. In this study, a shear-responsive gel with a dual physically crosslinked network—combining hydrophobic association and $Fe^{3+}$-mediated ionic coordination—was prepared through a single-step water-based radical polymerization process, utilizing commercially available monomers. By systematically tuning the hydrophobic monomer and $Fe^{3+}$ contents, the gel's fracture-sealing efficacy, autogenous healing ability, and shear rheological characteristics were evaluated, establishing a quantitative correlation between the critical shear rate and drilling parameters. The empirical data demonstrate that with an increase in the hydrophobic monomer dosage from 0.4 wt% to 1.2 wt%, the critical shear rate decreases from 22.5 $s^{-1}$ to 8.6 $s^{-1}$, exhibiting an exponential decay relationship. The optimized formulation, G0.8F0.5, demonstrates a low initial viscosity of 245 mPa·s under high shear conditions, which surges to 6180 mPa·s at a shear rate of 14.2 $s^{-1}$, achieving a thickening factor of 29.4. Upon incubation at 80 °C for a duration of 12 h, the formulated gel restores 94.9% of its mechanical tensile strength and 96.3% of its fracture strain, whereas the $Fe^{3+}$-free control sample fails to heal. In dynamic plugging tests using a 3 mm fracture plate, G0.8F0.5 achieves a breakthrough pressure of 12.8 MPa with a minimal fluid loss of 98 mL. The LCM forms a monolithic gel block positioned at the middle-to-rear section of the fracture, outperforming conventional gel counterparts. Drilling hydraulics simulations reveal that deploying this gel reduces the annular equivalent circulating density (ECD) by 0.06 g/$cm^3$. Furthermore, under idealized conditions, this approach is calculated to enhance the ROP by approximately 26%. The proposed molecular design of a shear-responsive, dual physically crosslinked network provides a viable technical pathway for quantitatively tailoring the shear-responsive properties of while-drilling LCMs.

**Keywords:** rate of penetration enhancement; gel-based lost circulation material; shear responsiveness; hydrophobic association; ionic coordination



Academic Editor: Dicho Stratiev

Received: 27 May 2026
Revised: 12 June 2026
Accepted: 23 June 2026
Published: 3 July 2026

## 1. Introduction

During well operations in naturally fractured strata, drilling fluid loss stands out as a ubiquitous downhole challenge. This phenomenon not only leads to the severe depletion of drilling muds and lost circulation materials (LCMs), but also poses a severe risk of triggering catastrophic incidents such as wellbore collapse, pipe sticking, and blowouts [1,2]. Global industry data reveals that more than a quarter of petroleum wells suffer from fluid leakage, with the ensuing non-productive time (NPT) accounting for more than 70% of downhole complexity-related delays [3]. As petroleum exploration continuously advances toward deep-lying and highly heterogeneous reservoirs, controlling lost circulation in macro-fractures becomes increasingly critical. Over the decades, LCMs have evolved from conventional particulate bridging agents (e.g., walnut shells, calcium carbonate) to high-fluid-loss squeezes, and recently, to polymer gels and curable resins [4,5]. Among these, polymer gels have garnered considerable attention owing to their exceptional deformability, which allows them to adapt to varying and irregular fracture geometries that rigid particulates fail to seal. Furthermore, the in situ sealing process within these irregular downhole channels is highly intricate, often involving non-Darcy seepage dynamics in post-failure rocks and complex solid–fluid phase interactions. Recent advanced analytical approaches, such as bifurcation dynamical analysis and CFD-DEM coupling models, have provided profound theoretical frameworks for understanding the flow and accumulation mechanisms of grouting slurries within rough fractures [6,7]. These cutting-edge perspectives highlight the paramount necessity of designing LCMs with highly adaptive rheological properties.

Despite their morphological adaptability, traditional supramolecular gel LCMs inherently suffer from a fundamental contradiction. On the one hand, maintaining a high crosslinking density ensures a dense sealing layer and high breakthrough pressure post-placement; on the other hand, this high initial viscosity drastically elevates circulating friction during pumping, severely restricting pumpability [5,8,9]. To circumvent this, Shear-Thickening Fluids (STFs)—typically physical dispersion systems like nanosilica/polyethylene glycol—have been introduced, offering the novel concept of "fracture-triggered thickening" [10,11]. STFs maintain low viscosity under low shear but exhibit exponential viscosity surges under specific shear fields. However, these purely physical dispersions lack a robust chemically crosslinked network, rendering their self-healing capabilities highly deficient; consequently, STF seals are extremely brittle and susceptible to structural failure under downhole pressure fluctuations [12–14]. Conversely, researchers have synthesized autonomous self-healing gels relying on dynamic bonds. While these materials exhibit excellent structural regeneration post-rupture, current studies have overwhelmingly focused on their static healing kinetics under varying temperatures, leaving their dynamic shear-responsive rheology—specifically how they flow and transition under extreme wellbore shear rates—largely underexplored [15–17].

This leads to the core scientific gap in contemporary LCM design: the persistent paradox between "pumpability inside the drill string" and "in-situ retention inside the fracture" [18,19]. A fundamental conceptual flaw in previous studies is the reliance on static time-delayed gelation, completely ignoring the dynamic spatial variations in shear rates—from >100 $s^{-1}$ inside the bit nozzles to ~10–20 $s^{-1}$ at the fracture inlet [20,21]. Consequently, their in-situ retention behavior lacks a design mechanism that is quantitatively correlated with drilling hydraulics. Therefore, concurrently achieving tunable shear-thickening (to resolve pumpability vs. retention) and robust self-healing (to ensure long-term seal integrity) within a single interpenetrating network remains an unresolved, yet highly promising, frontier [22,23].

Driven by the aforementioned challenges, this paper proposes a molecular design strategy for a shear-responsive, dual physically crosslinked gel. By employing acrylamide,

stearyl methacrylate, and 2-acrylamido-2-methylpropanesulfonic acid as the monomeric units, sodium dodecyl sulfate micelles and $Fe^{3+}$ ions were introduced via aqueous free-radical polymerization to construct a dual dynamic network comprising hydrophobic association and ionic coordination. Specifically, the hydrophobic association network imparts the shear-responsive characteristics, while the coordination bonds between $Fe^{3+}$ and sulfonic acid groups confer the self-healing capability. By systematically regulating the contents of the hydrophobic monomer and $Fe^{3+}$, the shear rheological behavior, self-healing performance, and fracture-plugging efficacy of the gel were comprehensively investigated, followed by the establishment of a quantitative correlation between the critical shear rate and drilling engineering parameters. Compared with existing research, the distinct novelties of this work lie in: (1) treating shear responsiveness as a tunable material parameter by tailoring the hydrophobic monomer content to align the critical shear rate with the specific shear rate window at the fracture inlet; (2) concurrently achieving shear thickening and self-healing within a single system, thereby overcoming the limitations of mono-functional materials; and (3) establishing a quantitative nexus between molecular parameters and rate of penetration (ROP) enhancement metrics, which establishes a rigorous conceptual framework for developing while-drilling LCMs.

## 2. Experimental Methods

### 2.1. Materials and Reagents

Acrylamide (AM), 2-acrylamido-2-methylpropanesulfonic acid (AMPS), stearyl methacrylate (SMA), sodium dodecyl sulfate (SDS), ammonium persulfate (APS), and iron(III) chloride hexahydrate ($FeCl_3 \cdot 6H_2O$), all of analytical grade with purities not less than 98%, were purchased from Shanghai Macklin Biochemical Co., Ltd. A conventional polyacrylamide-based gel lost circulation material, used as the control group (designated CG), was supplied by Western Drilling Engineering Company. To establish a scientifically valid baseline, CG is characterized as a covalently crosslinked polyacrylamide system synthesized via N,N′-methylenebisacrylamide (MBA), featuring an average pre-crosslinked molecular weight of approximately 6–8 million Da. Its network relies entirely on static, irreversible chemical bonds without any dynamically responsive coordination sites. Walnut shell particles (6–10, 10–20, 20–40, and 40–80 mesh) were obtained from Henan Tianyuan Petroleum Additives Co., Ltd.

### 2.2. Synthesis of the Gels

An aqueous one-pot free-radical polymerization strategy was employed for the fabrication of these gels. The basal formulation (based on the total mass of the reaction system) consisted of 12 wt% AM, 2 wt% AMPS, 1.5 wt% SDS, 0.3 wt% APS, and DI water as the balance. The mass fraction of SMA was systematically varied at 0.4%, 0.8%, and 1.2%, while the mass fraction of $Fe^{3+}$ (calculated as $FeCl_3 \cdot 6H_2O$) was set at 0%, 0.2%, and 0.5% (Table 1).

**Table 1.** Synthetic formulations and compositions of the gel samples.

| Sample | AM (wt%) | AMPS (wt%) | SMA (wt%) | SDS (wt%) | APS (wt%) | $Fe^{3+}$ (wt%) |
|---|---|---|---|---|---|---|
| G0.4F0.5 | 12 | 2 | 0.4 | 1.5 | 0.3 | 0.5 |
| G0.8F0 | 12 | 2 | 0.8 | 1.5 | 0.3 | 0 |
| G0.8F0.5 | 12 | 2 | 0.8 | 1.5 | 0.3 | 0.5 |
| G0.8F0.2 | 12 | 2 | 0.8 | 1.5 | 0.3 | 0.2 |
| G1.2F0.5 | 12 | 2 | 1.2 | 1.5 | 0.3 | 0.5 |

Synthesis Procedure: Predetermined amounts of AM, AMPS, and SDS were dissolved in DI water inside a 250 mL 3-neck spherical flask with a steady stirring rate of 200 r/min until a homogeneous solution formed. SMA, pre-liquefied in a 60 °C water bath, was added dropwise into the reaction medium. Concurrently, the agitation rate was elevated to 400 r/min, and the resulting blend was maintained for 30 min to facilitate the formation of solubilized micelles. Subsequently, $FeCl_3 \cdot 6H_2O$ was introduced into the system and stirred for an additional 15 min. Finally, APS was incorporated as the radical initiator, after which the solution was deoxygenated by purging with high-purity nitrogen for 15 min. The flask was then hermetically sealed and submerged in a thermostatic water bath at 60 °C for 4 h to allow polymerization.

Upon completion, the resultant hydrogels were collected, sectioned into approximately 1 $cm^3$ cubes, and desiccated in a vacuum oven at 60 °C for 24 h. The dried gels were pulverized and consecutively sieved through 8-, 10-, 20-, 40-, and 80-mesh standard sieves to yield four specific particle-size ranges: 8–10 mesh, 10–20 mesh, 20–40 mesh, and 40–80 mesh. These categorized particles were stored in airtight containers for subsequent evaluations.

### *2.3. Structural Characterization*

Fourier Transform Infrared (FTIR) Spectroscopy: Spectra were recorded on a Bruker Tensor 27 spectrometer utilizing KBr pellets. Scans were acquired from 400 to 4000 $cm^{-1}$ with a resolution of 2 $cm^{-1}$ (32 scans/sample).

Thermogravimetric Analysis (TGA): TGA curves were acquired via a Netzsch STA-449-F3 instrument ($N_2$ flow: 50 mL/min, 30–600 °C, 10 °C/min) to extract the initial degradation temperature ($T_{5\%}$), maximum decomposition rate temperature ($T_{peak}$), and final residual yields of ~10 mg samples.

Dynamic Mechanical Analysis (DMA): Viscoelastic profiles ($E'$, and $T_g$ indicated by tan δ) were characterized using a TA Q800 apparatus (single-cantilever mode). Pre-swollen, 80 °C-cured gel specimens (35 × 12 × 3 mm) were scanned from −80 to 150 °C (3 °C/min, 1 Hz, 0.1% strain).

Scanning Electron Microscopy (SEM): The gel samples were cryo-fractured in liquid nitrogen to preserve their network structures. The exposed cross-sections were mounted upward on conductive stubs, sputter-coated with gold (15 mA, 90 s), and examined using a Hitachi SU8220 field-emission SEM at an accelerating voltage of 5 kV and a working distance of 8–10 mm. ImageJ software was employed to statistically determine the average pore diameter, pore wall thickness, and spherical node dimensions by analyzing a minimum of 50 pores per image.

### *2.4. Rheological Measurements*

Rheological characterizations were executed using an Anton Paar MCR 302 rotational rheometer equipped with a parallel-plate geometry (25 mm diameter) and a precisely set gap of 1 mm. Gel particles pre-swollen in a 4 wt% bentonite slurry at 60 °C for 4 h were carefully loaded onto the lower stationary plate. The upper plate was lowered, excess material was trimmed, and a solvent trap was mounted to mitigate evaporation. The testing temperature was maintained at 60 °C. To erase any mechanical history, a steady pre-shear (1 $s^{-1}$) was applied for 1 min prior to the actual measurements.

Steady-Shear Testing: Viscosity profiles ($\eta$ vs. $\gamma$) were generated via logarithmic sweeps (0.1–500 $s^{-1}$, 10 points/decade, 10 s integration time per point). Several critical rheological signatures were extracted from these curves: initial viscosity ($\eta_0$ at 0.1 $s^{-1}$), the onset shear rate of thickening ($\dot{\gamma}_c$), extreme viscosity values ($\eta_{min}$ and $\eta_{max}$), the shear rate at peak viscosity ($\dot{\gamma}_{max}$), and the overall thickening factor ($\eta_{max}/\eta_{min}$). All measurements were performed in triplicate (values reported as mean ± SD). Herschel–Bulkley Modeling:

The empirical flow data were evaluated using nonlinear regression based on the Herschel–Bulkley rheological model ($\tau = \tau_0 + K\dot{\gamma}^n$). In this equation, $\tau$ represents the applied shear stress (Pa), $\tau_0$ is the yield stress (Pa), K is the consistency coefficient (Pa·s$^n$), $\dot{\gamma}$ is the shear rate (s$^{-1}$), and n is the dimensionless flow behavior index. This mathematical fitting mathematically quantifies the non-Newtonian fluid characteristics necessary for subsequent hydraulic simulations.

### 2.5. Self-Healing Performance Testing

Dried gel particles were pre-swollen in a 4 wt% bentonite slurry at 90 °C for 4 h, subsequently injected into dumbbell-shaped molds (Type 5A per GB/T 1040.2-2006), and conditioned at 90 °C for 12 h to form integral specimens. Upon demolding, the specimens were cleanly bifurcated transversely using a scalpel. The fractured surfaces were promptly realigned, pressed into physical contact, and incubated in an oven at 80 °C for varying healing durations (2, 4, 6, 8, 10, 12, 16, and 24 h).

Uniaxial tensile tests were performed on an MTS CMT4204 universal testing machine with an initial gauge length of 50 mm and a crosshead speed of 50 mm/min. Tensile strength ($\sigma$) and elongation at break ($\varepsilon$) for both pristine (uncut) and healed specimens were recorded. Healing efficiencies were evaluated as $\eta_1 = (\sigma_{healed}/\sigma_{original}) \times 100\%$ and $\eta_2 = (\varepsilon_{healed}/\varepsilon_{original}) \times 100\%$. Five replicate tests were conducted for each condition, with results reported as mean ± standard deviation.

### 2.6. Swelling Performance Testing

Approximately 0.5 g of dried gel particles was precisely weighed ($M_0$, ±0.001 g) and submerged in 100 mL of 4 wt% bentonite slurry within a 200 mL beaker placed in a 90 °C thermostatic water bath. At predetermined intervals, the swollen particles were extracted, briefly blotted with filter paper to remove superficial liquid, and gravimetrically assessed ($M_t$) before rapid re-immersion. Equilibrium was deemed established when the mass variation between successive weighings fell below 0.005 g, recorded as $M_e$. The swelling degree ($Q$) was calculated by $Q = (M_t - M_0)/M_0$. Each sample formulation was evaluated in triplicate.

### 2.7. Fracture Plugging Performance Testing

A DLM-01 dynamic lost circulation simulator was employed in conjunction with a custom-built steel tapered fracture plate. The LCM slurry was prepared by dispersing 5 wt% of gel particles (formulated in a multi-modal size distribution: 25 wt% of 8–10 mesh, 45 wt% of 10–20 mesh, and 30 wt% of 20–40 mesh) into a 4 wt% bentonite slurry and agitating for 30 min. The formulated slurry was transferred to the fluid reservoir of the simulator, and the fracture module was securely fastened. Commencing with an initial injection pressure of 0.5 MPa and a flow rate of 5 mL/min, the effluent characteristics were continuously monitored. If continuous fluid breakthrough occurred, the cumulative fluid loss was documented. Conversely, if a seal formed, the pressure was elevated in increments of 0.5 MPa every 2 min until seal failure (manifested by continuous effluent), at which point the maximum sustained pressure was designated as the breakthrough pressure. A minimum of three trials were conducted per formulation. Post-test, the fracture plate was disassembled to measure and photograph the penetration depth and total length of the formed plugging layer.

To assess dimensional adaptability, identically prepared G0.8F0.5 slurries were evaluated against fracture plates with varying inlet widths (1, 2, 3, 4, and 5 mm). The temporal relationship between injection pressure and fluid loss rate was meticulously recorded to decipher the sequential formation mechanism of the plugging slug.

### 2.8. Drilling Hydraulics Simulation

Leveraging the empirically derived Herschel–Bulkley parameters ($\tau_0$, $K$, n), drilling hydraulics were numerically simulated via DrillHydraulics v2.0 software. The overall calculation procedure in the software strictly adheres to the API RP 13D guidelines for non-Newtonian fluid hydraulics [24]. The simulation operates under the fundamental assumptions of steady-state flow, an incompressible fluid, and a concentric wellbore annulus. The predefined wellbore architecture parameters were as follows: well depth = 6500 m, horizontal section length = 2500 m, drill pipe OD = 127 mm, casing ID = 215.9 mm, drilling fluid density = 1.40 g/cm$^3$, pump rate = 30 L/s, and bit nozzle diameter = 12 mm (3 nozzles). Upon inputting the respective rheological parameters of each gel sample, the software computed the annular pressure drop ($\Delta P_{ann}$, MPa), the equivalent circulating density (ECD, g/cm$^3$), and the bit hydraulic horsepower (HHP, kW). Setting the conventional gel (CG) as the baseline reference (Relative ROP = 100%), the relative rate of penetration (ROP) for the experimental gels was predicted using the established empirical correlation (ROP $\propto$ HHP^0.4). Furthermore, parametric sensitivity regarding pump rates (20, 25, 30, 35, and 40 L/s) was analyzed specifically for G0.8F0.5 to correlate flow dynamics with annular pressure drop and ECD.

## 3. Results and Discussion

### 3.1. Molecular Structure Characterization

The FTIR spectra of the six synthesized samples are illustrated in Figure 1a. All specimens exhibited a broad and intense absorption band near 3345 cm$^{-1}$, reflecting the simultaneous stretching vibrations of both O–H and N–H functionalities. Observed at 2929 cm$^{-1}$ and 2850 cm$^{-1}$, the moderately intense signals represent the asymmetric and symmetric stretching modes of aliphatic –$CH_2$– and –$CH_3$ functionalities from SMA, confirming that the hydrophobic monomer was successfully integrated into the polymer chain. The ester C=O stretching from the SMA units manifests as a shoulder signal at 1728 cm$^{-1}$, while the prominent absorption at 1645 cm$^{-1}$ originates from the amide carbonyl stretching mode. Notably, the four $Fe^{3+}$-incorporated samples, namely G0.4F0.5, G0.8F0.5, G0.8F0.2, and G1.2F0.5, displayed a newly emerging peak at approximately 560 cm$^{-1}$. This peak is characteristic of the stretching vibration of the Fe–O coordination bond and was absent in the $Fe^{3+}$-free G0.8F0 sample and the conventional gel (CG). Simultaneously, the $Fe^{3+}$-loaded specimens displayed the typical signatures of sulfonic acid (–$SO_3^-$) moieties at 1175–1177 cm$^{-1}$ and 1034–1036 cm$^{-1}$. Compared to the G0.8F0 baseline at 1180/1040 cm$^{-1}$, these peaks exhibited a redshift of approximately 4–6 cm$^{-1}$ along with slight peak broadening. This spectral shift is attributed to the coordination interaction between $Fe^{3+}$ and –$SO_3^-$, which altered the electron cloud density surrounding the sulfonic acid groups. The combined evidence firmly validates that $Fe^{3+}$ ions have successfully coordinated with the AMPS-derived sulfonic functionalities to construct ionic linkages. A widened N–H absorption region emerged at 3420 cm$^{-1}$ alongside an amide C=O signal at 1650 cm$^{-1}$ for the CG specimen, yet it lacked both the 560 cm$^{-1}$ coordination peak and the 2929/2850 cm$^{-1}$ alkyl characteristic peaks, an observation perfectly aligning with a standard polyacrylamide structure.

Figure 1b delineates the TGA traces used to investigate the thermal endurance of the gel systems, revealing a tripartite degradation pathway for each formulation. Specifically, the early-stage mass drop (spanning 30 °C to 220 °C) was predominantly caused by the removal of non-bound and coordinated water. Here, the extent of weight reduction for the $Fe^{3+}$-loaded networks amounted to 6–8%, marginally higher than the 5% observed for G0.8F0, as the ionic coordination enhanced the overall hydrophilicity and consequently elevated the bound water content. The CG sample exhibited a weight loss of approxi-

mately 7% within this regime. The subsequent temperature window spanning 220 °C to 400 °C corresponds to the main structural breakdown of the polymeric network. The G0.8F0 experienced a decomposition peak at roughly 265 °C, induced by the pyrolysis and dehydration of the pendant amide groups to form imine structures. The decomposition peak temperature for G0.8F0.5 shifted to approximately 278 °C, suggesting that the $Fe^{3+}$ coordination bonds imparted greater rigidity to the macromolecular chains and elevated the thermal decomposition activation energy. For G1.2F0.5, this peak temperature further advanced to 285 °C, demonstrating that a denser hydrophobic association network additionally benefits thermal stability. Conversely, the CG sample recorded the lowest decomposition peak temperature at 258 °C. A similar trend was observed for the 5% weight loss temperature designated as $T_{5\%}$: the values were recorded as 226 °C for G0.8F0, 232 °C for G0.8F0.5, 235 °C for G1.2F0.5, and a mere 210 °C for CG. It is evident that the thermal robustness of these samples benefits significantly from the addition of $Fe^{3+}$ as well as the heightened SMA levels, with $Fe^{3+}$ contributing a temperature elevation of about 6 °C and the increase in SMA from 0.8 wt% to 1.2 wt% contributing approximately 3 °C. The final stage, spanning 400 °C to 550 °C, corresponds to the cleavage and decomposition of the polymer's carbon–carbon backbone. All samples exhibited a broad decomposition peak near 420 °C. At 600 °C, the residual mass fractions for G0.8F0.5 and G1.2F0.5 were 10.5% and 10.0%, respectively, surpassing those of G0.8F0 at 8.0% and CG at 3.5%. These final residues primarily consist of metal oxide and sulfide complexes formed by $Fe^{3+}$ and the sulfonic groups. Overall, the thermal stability of the investigated samples followed the sequence: G1.2F0.5 ≈ G0.8F0.5 > G0.8F0.2 > G0.4F0.5 > G0.8F0 > CG.

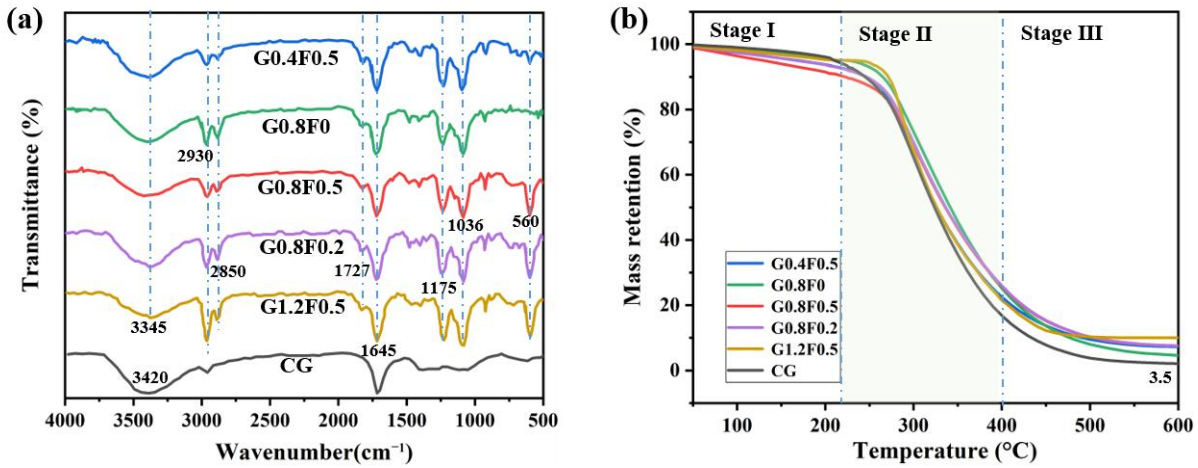


**Figure 1.** Structural and thermal characterization of the gel samples. (**a**) FTIR spectra; (**b**) TGA curves.

Figure 2 tracks the temperature-dependent evolution of both the storage modulus and loss tangent for the prepared samples. Notably, the curves exhibit an evident transition peak in the range of −60 °C to −30 °C, signifying the vitrification-to-rubber transition of the soft segments, denoted herein as $T_{g,soft}$. The $T_{g,soft}$ values for G0.8F0 and G0.8F0.5 were −48 °C and −45 °C respectively; this slight elevation signifies that the $Fe^{3+}$ coordination bonds restricted segmental motion. The $T_{g,soft}$ for G1.2F0.5 further increased to −42 °C, aligning with an augmented crosslinking density. In contrast, the CG sample exhibited a lower $T_{g,soft}$ of −50 °C compared to its $Fe^{3+}$-containing counterparts. Within the higher temperature range of 80 °C to 120 °C, the $Fe^{3+}$-incorporated gels, including G0.8F0.5 and G1.2F0.5, exhibited a secondary tan δ peak, an attribute barely discernible in both G0.8F0 and CG. This high-temperature transition corresponds to the glass transition of the hard-segment phase denoted as $T_{g,hard}$, which was approximately 92 °C for G0.8F0.5 and 95 °C for G1.2F0.5. The manifestation of this peak serves as direct evidence that the ionic

coordination sites and the hydrophobic association domains segregated into independent hard-segment micro-domains, thereby confirming the occurrence of microphase separation. Such an appropriate degree of microphase separation is highly conducive to chain segment diffusion and the reconstruction of crosslinking sites during the self-healing process. At ambient temperature (25 °C), G0.8F0.5 demonstrated a storage modulus E′ of $1.0 \times 10^6$ Pa, outperforming both G0.8F0 at $0.7 \times 10^6$ Pa and CG at $0.5 \times 10^6$ Pa. Notably, at an elevated temperature of 80 °C approaching the healing conditions, G0.8F0.5 maintained an E′ of $0.23 \times 10^6$ Pa, preserving favorable structural integrity, whereas the CG sample suffered substantial thermal softening with an E′ plunging to $0.12 \times 10^6$ Pa.

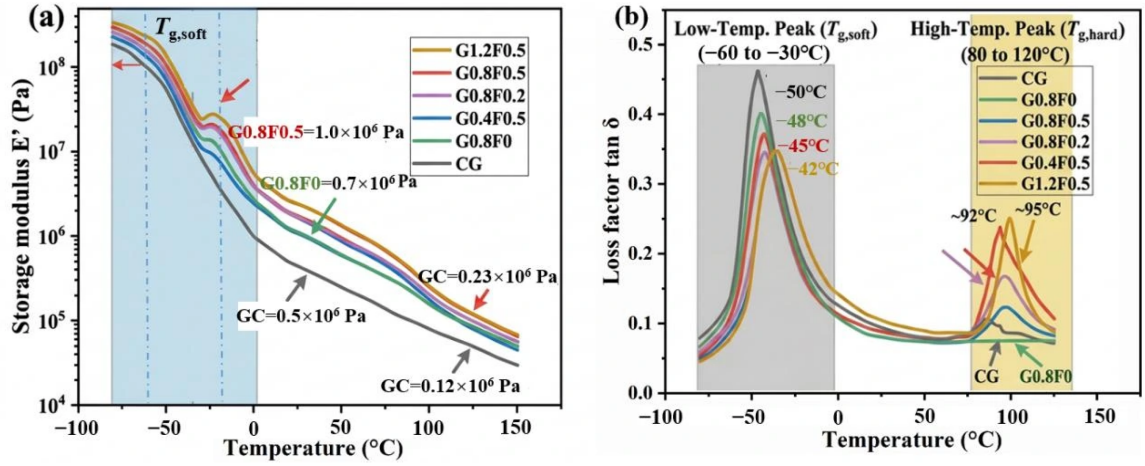


**Figure 2.** Dynamic mechanical analysis of the gel formulations. (**a**) Storage modulus (E′) evolution with temperature (°C). (**b**) Loss tangent (tan δ) evolution with temperature.

The microstructural disparities were visually captured via SEM, as shown in Figure 3. The $Fe^{3+}$-free G0.8F0 sample displayed a loose three-dimensional network characterized by large, unevenly distributed pores, thin pore walls, and a generally sparse structural skeleton. Conversely, the macromolecular architecture of G0.8F0.5 was distinctly densified. It featured significantly diminished pore dimensions, thickened pore walls, and a highly continuous and robust network skeleton, culminating in exceptionally compact morphological characteristics. This visual evidence verifies that the introduction of $Fe^{3+}$ effectively transitions the hydrogel from a highly porous, relaxed state to a densely packed, continuous network, laying the essential structural groundwork for subsequent shear-thickening and self-healing functionalities.

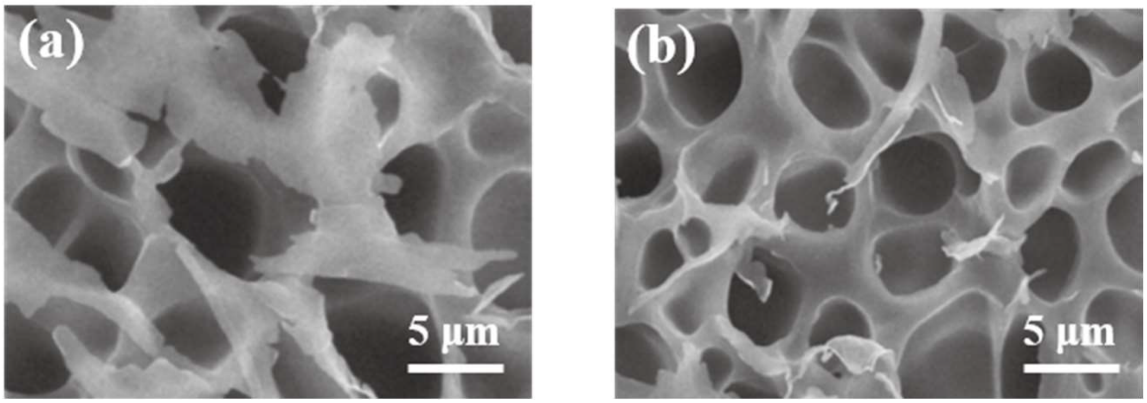


**Figure 3.** Cross-sectional SEM micrographs of (**a**) G0.8F0 and (**b**) G0.8F0.5.

### 3.2. Shear Rheological Behavior

Steady-shear rheological evaluations, detailed in Figure 4 and Table 2, revealed that all four $Fe^{3+}$-incorporated variants, including G0.4F0.5, G0.8F0.5, G0.8F0.2, and G1.2F0.5, exhibited a distinct triphasic rheological profile comprising low-shear thinning, intermediate-shear thickening, and high-shear secondary thinning regimes. This complex fluid dynamic is fundamentally governed by a shear-induced association mechanism inherent to hydrophobically modified polymers. Under low-shear conditions, the hydrophobic micelles function as temporary physical crosslinkers sustaining the network; however, as the shear stress escalates, these micelles orient and undergo dissociation, resulting in a decline in viscosity. Once the shear rate intercepts a critical threshold designated as $\dot{\gamma}_c$, the polymer chains are forcibly stretched and oriented. This conformational extension exposes previously buried hydrophobic blocks, which rapidly formulate transient intermolecular associations to construct a densely intertwined network, triggering a precipitous surge in viscosity. Upon applying even more aggressive shear forces, these transient associations are ultimately ruptured, precipitating a secondary shear-thinning phase. However, the emergence of this secondary shear-thinning phenomenon poses a potential operational risk. It indicates that the macroscopic physical network possesses an ultimate tolerance limit. If the localized shear rate induced by extreme high-flow-rate fluid scouring inside the fracture exceeds this critical threshold, the rupture rate of the dynamic reversible bonds will surpass their re-association rate [25]. Consequently, this could lead to irreversible structural degradation and subsequent washout of the established plugging layer under severe downhole conditions.

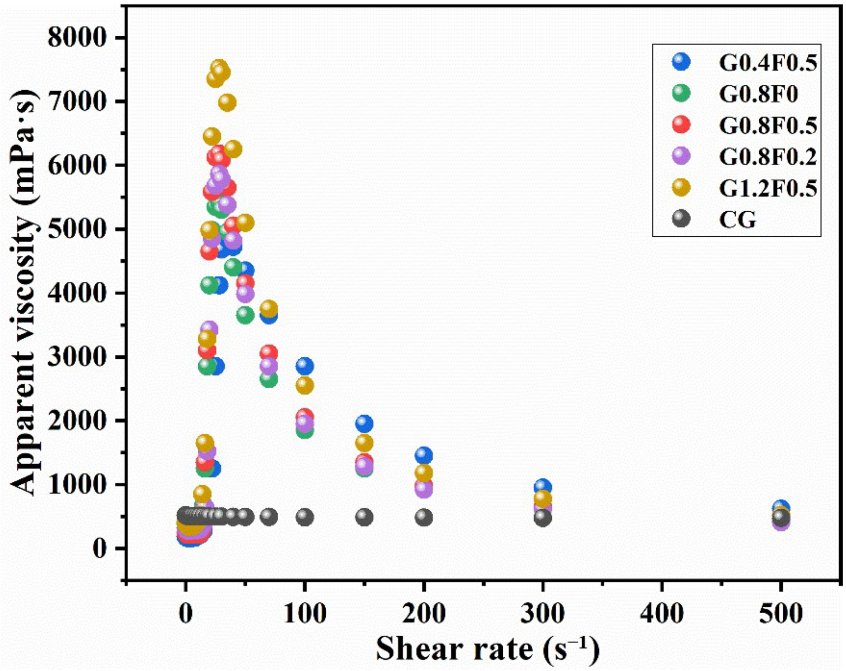


**Figure 4.** Dependence of apparent viscosity on shear rate for the prepared gel networks at a constant temperature of 60 °C.

**Table 2.** Shear-thickening parameters of gels with varying SMA contents ($Fe^{3+}$ = 0.5 wt%, 60 °C).

| Sample | SMA/% | $\dot{\gamma}_c$ ($s^{-1}$) | $\eta_0$ (mPa·s) | $\eta_{min}$ (mPa·s) | $\eta_{max}$ (mPa·s) | $\dot{\gamma}_{max}$ ($s^{-1}$) | Thickening Factor |
|---|---|---|---|---|---|---|---|
| G0.4F0.5 | 0.4 | 22.5 | 185 | 162 | 4850 | 35 | 29.9 |
| G0.8F0.5 | 0.8 | 14.2 | 245 | 210 | 6180 | 28 | 29.4 |
| G1.2F0.5 | 1.2 | 8.6 | 410 | 338 | 7520 | 28 | 22.2 |

In stark contrast, the $Fe^{3+}$-free G0.8F0 sample displayed a considerably muted shear-thickening capability, yielding a maximum viscosity of 5420 mPa·s alongside a limited thickening index of 17.2, lacking a discernible $\dot{\gamma}_c$ inflection point. This suggests that a purely hydrophobically associated network is highly susceptible to unmitigated dissociation under shear fields, hindering the formation of a robust transient network. The CG reference behaved predominantly as a Newtonian fluid with a steady viscosity spanning 488–518 mPa·s and a flow index near 0.98, perfectly mirroring its covalently and permanently crosslinked nature.

A critical observation is the inverse relationship between the critical shear rate $\dot{\gamma}_c$ and the SMA concentration: $\dot{\gamma}_c$ reduced from 22.5 $s^{-1}$ for G0.4F0.5, down to 14.2 $s^{-1}$ for G0.8F0.5, and further to 8.6 $s^{-1}$ for G1.2F0.5. This correlation confirms that manipulating the hydrophobic monomer dosage allows for precise tuning of the shear-response triggering threshold, presenting an invaluable engineering tool to synchronize the material's behavior with specific fracture-inlet shear rates downhole. Although the maximum attainable viscosity enhanced proportionally with SMA addition, reaching 7520 mPa·s for G1.2F0.5, the thickening factor of this highly modified variant dropped to 22.2, inferior to the 29.4 ratio of G0.8F0.5. This discrepancy arises because the excessively high initial viscosity of G1.2F0.5 at 410 mPa·s substantially restricted the available margin for viscosity multiplication. From an operational fluid-dynamics perspective, shear rates across drill bit nozzles and annular return zones typically exceed 100 $s^{-1}$, whereas cross-sectional contraction effects at the fracture inlet decelerate the fluid shear to approximately 10–20 $s^{-1}$. It is worth noting that this fracture-inlet shear rate was analytically estimated based on the classical Newtonian flow model through a parallel-plate slot ($\dot{\gamma} = 6Q/wh^2$, where $Q$ is flow rate, $w$ is fracture width, and $h$ is fracture height), derived directly from the pump injection parameters of our dynamic plugging apparatus [26]. The optimized $\dot{\gamma}_c$ of 14.2 $s^{-1}$ for G0.8F0.5 aligns flawlessly with this critical window. It ensures a low pumpable viscosity of 245 mPa·s within the drill string while activating a robust shear-thickening response up to 6180 mPa·s immediately upon penetrating the fracture. In contrast, the elevated $\dot{\gamma}_c$ of G0.4F0.5 prevents activation at the fracture entrance, leading to excessive depth migration and insufficient plugging; conversely, the overly sensitive G1.2F0.5 triggers premature thickening, resulting in undesirable particulate accumulation right at the inlet. These rheological predictions were subsequently corroborated by dynamic plugging experimental data.

Evaluating the rheological impact of varying $Fe^{3+}$ concentrations among G0.8F0, G0.8F0.2, and G0.8F0.5 as presented in Table 3 uncovers the critical role of ionic crosslinking. The uncoordinated G0.8F0 registered an elevated low-shear viscosity of 380 mPa·s coupled with a weak shear-thickening profile. Introducing 0.2 wt% $Fe^{3+}$ reduced the initial viscosity to 318 mPa·s, established a $\dot{\gamma}_c$ of 16.5 $s^{-1}$, elevated the peak viscosity to 5860 mPa·s, and boosted the thickening factor from 16.7 to 21.3. Maximizing the $Fe^{3+}$ dosage to 0.5 wt% further depressed the low-shear viscosity to 245 mPa·s, shifted $\dot{\gamma}_c$ favorably to 14.2 $s^{-1}$, pushed the peak viscosity to 6180 mPa·s, and achieved an exceptional thickening factor of 29.4. This bidirectional enhancement executed by $Fe^{3+}$ operates via dual mechanisms. Primarily, the ionic coordination bridges between $Fe^{3+}$ and sulfonic acid groups induce a mild macroscopic contraction of the quiescent network, thus diminishing the low-shear flow resistance. Secondarily, given that the bond energy of ionic coordination at 200–400 kJ/mol massively overshadows the 10–30 kJ/mol of hydrophobic associations, these coordination sites act as robust "elastic buffers" under high-shear duress. They effectively prevent the catastrophic unraveling of the molecular network, thereby profoundly magnifying the shear-thickening amplitude [27].

**Table 3.** Shear rheological parameters of gels with varying $Fe^{3+}$ contents (SMA = 0.8 wt%, 60 °C).

| Sample | $Fe^{3+}$ (%) | $\dot{\gamma}_c$ ($s^{-1}$) | $\eta_0$ (mPa·s) | $\eta_{min}$ (mPa·s) | $\eta_{max}$ (mPa·s) | Thickening Factor |
|---|---|---|---|---|---|---|
| G0.8F0 | 0 | — | 380 | 315 | 5420 | 17.2 |
| G0.8F0.2 | 0.2 | 16.5 | 318 | 275 | 5860 | 21.3 |
| G0.8F0.5 | 0.5 | 14.2 | 245 | 210 | 6180 | 29.4 |

### *3.3. Self-Healing Performance*

The incorporation of F $Fe^{3+}$ proved to be the indispensable catalyst for intrinsic self-healing capabilities, as evidenced by the tensile recovery profiles in Figure 5. The bisected surfaces of the $Fe^{3+}$-free G0.8F0 completely failed to heal, instantly separating upon minimal manipulative stress post-incubation. For G0.8F0.2, the tensile strength recovery efficiency designated as $\eta_1$ reached 63.6%; however, the regenerated specimen ruptured precisely at the original bisection interface, leaving visually discernible structural defects. Remarkably, G0.8F0.5 achieved an outstanding $\eta_1$ of 94.9%, with subsequent mechanical failure manifesting exclusively within the pristine bulk material rather than the healed interface, alongside an elongation-at-break recovery efficiency $\eta_2$ of 96.3%. Thus, elevating the $Fe^{3+}$ concentration from 0.2 wt% to 0.5 wt% catalyzed a striking 31 percentage point improvement in healing efficacy. Expectedly, the covalently crosslinked CG sample demonstrated zero regenerative capacity. The underlying mechanism hinges on the $Fe^{3+}$-sulfonate coordination bonds providing instantaneous physical anchoring, which immediately generates sufficient interfacial adhesion upon physical contact. Subsequently, propelled by the 80 °C thermal stimulus, polymer segments actively diffuse across the interface, initiating the reconstruction of hydrophobic association nodes. Concurrently, the reversible dissociation and recombination of the ionic coordination bonds facilitate a homogenous redistribution of crosslinking junctions, ultimately culminating in full dual-network reconstruction and comprehensive mechanical restoration. In the absence of $Fe^{3+}$, relying exclusively on hydrophobic re-association generates adhesion forces too weak to sustain structural integrity.

The temporal evolution of $\eta_1$ for G0.8F0.5 progressed through three distinct kinetic stages. Stage I from 0 to 2 h yielded an $\eta_1$ of 32.5%, providing minimal load-bearing capacity primarily driven by rapid interfacial $Fe^{3+}$-sulfonate coordination. Stage II, spanning 2–8 h, witnessed a rapid surge in healing efficiency, soaring to 72.8% by hour 6 and exhibiting prominent necking phenomena during elongation; this phase was dominated by extensive macromolecular chain diffusion and the re-establishment of hydrophobic domains [28]. Stage III from 8 to 12 h marked a deceleration in recovery kinetics, plateauing at 94.9% at the 12 h mark and marginally climbing to 95.8% after 24 h, an era governed by the spatial redistribution of ionic bonds and final network densification.

A comparative assessment based on hydrophobic modification levels revealed that the 94.9% strength recovery of G0.8F0.5 substantially overshadowed the 85.3% of G0.4F0.5 and the 88.6% of G1.2F0.5. The sparsely modified G0.4F0.5 suffered from a deficit of hydrophobic anchoring sites, resulting in substandard interfacial network reconstruction. Conversely, the hyper-associated matrix of G1.2F0.5 severely restricted post-healing ductility, yielding an inferior $\eta_2$ of 79.2%. A meticulously calibrated hydrophobic density utilizing 0.8 wt% SMA strikes an optimal balance, furnishing an abundance of crosslinking nodes without inducing severe steric hindrance against segmental mobility.

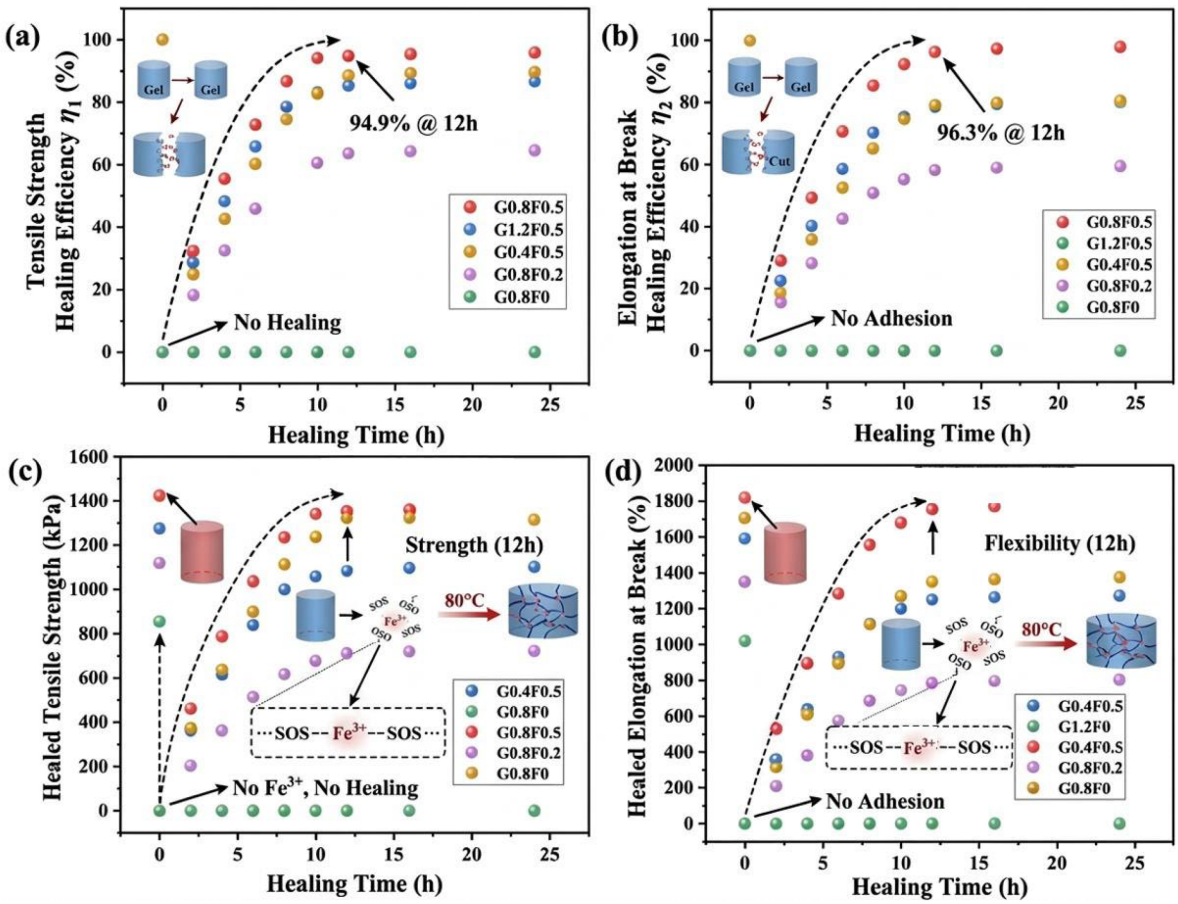


**Figure 5.** Self-healing performance. (**a**) Tensile strength healing efficiency over time. (**b**) Elongation healing efficiency over time. (**c**) Tensile strength recovery at 12 h. (**d**) Elongation recovery at 12 h.

Synthesizing these empirical findings, the self-healing paradigm of G0.8F0.5 operates via three synergistic phases: (1) Physical anchoring: Immediate interfacial adhesion is secured via the rapid regeneration of $Fe^{3+}$-sulfonate coordination bonds upon contact, achieving 32.5% recovery within 2 h. (2) Network reconstruction: Thermally activated segment diffusion at 80 °C promotes the reassembly of hydrophobic micelles across the boundary, while the dynamic nature of ionic bonds ensures uniform crosslink distribution, elevating recovery to 86.7% by hour 8. (3) Strength recovery: The fully reconstructed interpenetrating dual network fully reclaims its mechanical prowess, solidifying a 94.9% strength recovery post 12 h. Comparisons against both the unmodified G0.8F0 and the conventional CG unequivocally prove that while ionic coordination serves as the absolute prerequisite for initiating self-healing, the dynamic reversibility of the hydrophobic network guarantees the restoration of post-healing toughness. The seamless synergy between these two dynamically reversible crosslinking modalities empowers G0.8F0.5 with not only near-perfect strength recuperation but also an exceptional 96.3% retention of its original elongation limits.

While the current evaluations at 60–90 °C and atmospheric pressure establish the gel's baseline physical chemistry, applying it to ~6500 m deep wells entails harsher conditions. Extremely high temperatures (>130–150 °C) may compromise micelle thermodynamics and accelerate $Fe^{3+}$ hydrolysis, while confining pressures and formation fluids could alter the network reconstruction kinetics [29]. Furthermore, field applicability demands compatibility with complex drilling muds; high salinity or extreme pH may shield ionic coordination, whereas weighting agents and polymers might sterically hinder hydrophobic re-association. Consequently, evaluating the gel's performance under dynamic high-temperature, high-

pressure (HTHP) conditions and systematically assessing its compatibility with real-world mud systems remains a critical limitation of this study and will drive our future research.

### *3.4. Swelling Performance*

The swelling kinetics of the gel particles are depicted in Figure 6. An accelerated initial swelling was characteristic of all samples over the primary 4 h, preceding a decelerated growth rate between 4 and 8 h, ultimately achieving equilibrium after 12 h. Among all variants, the $Fe^{3+}$-free G0.8F0 sample attained the highest equilibrium swelling degree Q of 28.6 due to its minimal crosslinking density. The incorporation of $Fe^{3+}$ progressively restricted water absorption, driving Q down to 24.8 for G0.8F0.2 and 19.2 for G0.8F0.5. Similarly, augmenting the hydrophobic SMA content suppressed swelling, with Q dropping from 22.3 for G0.4F0.5 to 14.8 for G1.2F0.5. The conventional CG exhibited the lowest swelling capacity with a Q of 12.6. The intermediate Q value of 19.2 observed for G0.8F0.5, detailed in Table 4, is highly advantageous. Such moderate swellability permits the particles to expand sufficiently to seal inter-particle voids and densify the plugging layer. Simultaneously, the volume expansion of constrained particles within the fracture generates radial extrusion stress, thereby fortifying the overall structural integrity of the plug. Notably, G0.8F0.5 reached 80% of its equilibrium swelling capacity within 3.8 h. This timeframe synergizes perfectly with the 12 h healing period established in the fracture plugging tests, ensuring that the particles attain an optimal swollen volume precisely upon reaching the target plugging depth.

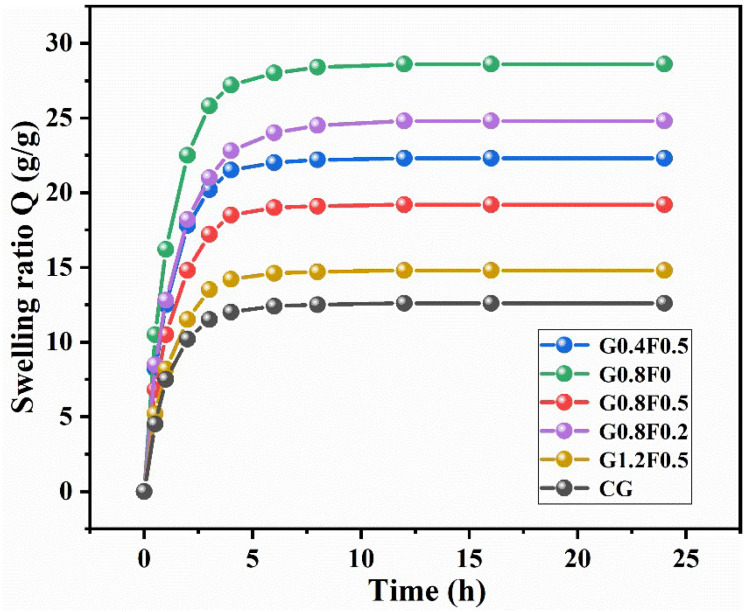


**Figure 6.** Temporal evolution of the swelling degree for various gel samples immersed in a 4 wt% bentonite slurry at 90 °C.

**Table 4.** Swelling parameters of gel samples in a 4 wt% bentonite slurry at 90 °C.

| Sample | Equilibrium Swelling Ratio Q | Time to Reach 80% Equilibrium (h) |
|---|---|---|
| G0.4F0.5 | 22.3 | 3.2 |
| G0.8F0 | 28.6 | 2.5 |
| G0.8F0.5 | 19.2 | 3.8 |
| G0.8F0.2 | 24.8 | 3.0 |
| G1.2F0.5 | 14.8 | 4.5 |
| CG | 12.6 | 5.0 |

### *3.5. Fracture Plugging Performance*

The sealing efficacies of the formulated slurries against a 3 mm tapered fracture are evaluated in Figure 7a,b. Pure walnut shells failed entirely to establish an effective seal resulting in total fluid loss, demonstrating that relying exclusively on rigid particulate bridging is inadequate for wedge-shaped fractures. The uncoordinated G0.8F0 formulation exhibited a meager breakthrough pressure of 5.8 MPa with a high fluid loss of 310 mL. Its resulting seal was localized superficially at the fracture mouth spanning 0–5 cm and remained completely unconsolidated, confirming that the absence of intrinsic self-healing is the primary catalyst for plugging failure. The CG reference achieved a breakthrough pressure of 7.2 MPa and restricted fluid loss to 215 mL; however, its seal relied merely on weak physical adsorption from the bentonite slurry and was entirely disintegrated upon breakthrough. In contrast, the optimally balanced G0.8F0.5 demonstrated superior performance, enduring an exceptional breakthrough pressure of 12.8 MPa with fluid loss curtailed to just 98 mL. It formed a cohesive, 15.6 cm long plugging layer situated deeply between 12 and 18 cm within the fracture. The remaining formulations yielded intermediate results: G0.4F0.5 and G0.8F0.2 recorded breakthrough pressures of 9.8 MPa and 8.5 MPa with corresponding fluid losses of 156 mL and 198 mL, yielding partially bonded seals. Although the hyper-modified G1.2F0.5 withstood 11.2 MPa, its resulting plug positioned at 8–16 cm was intact yet overly brittle.

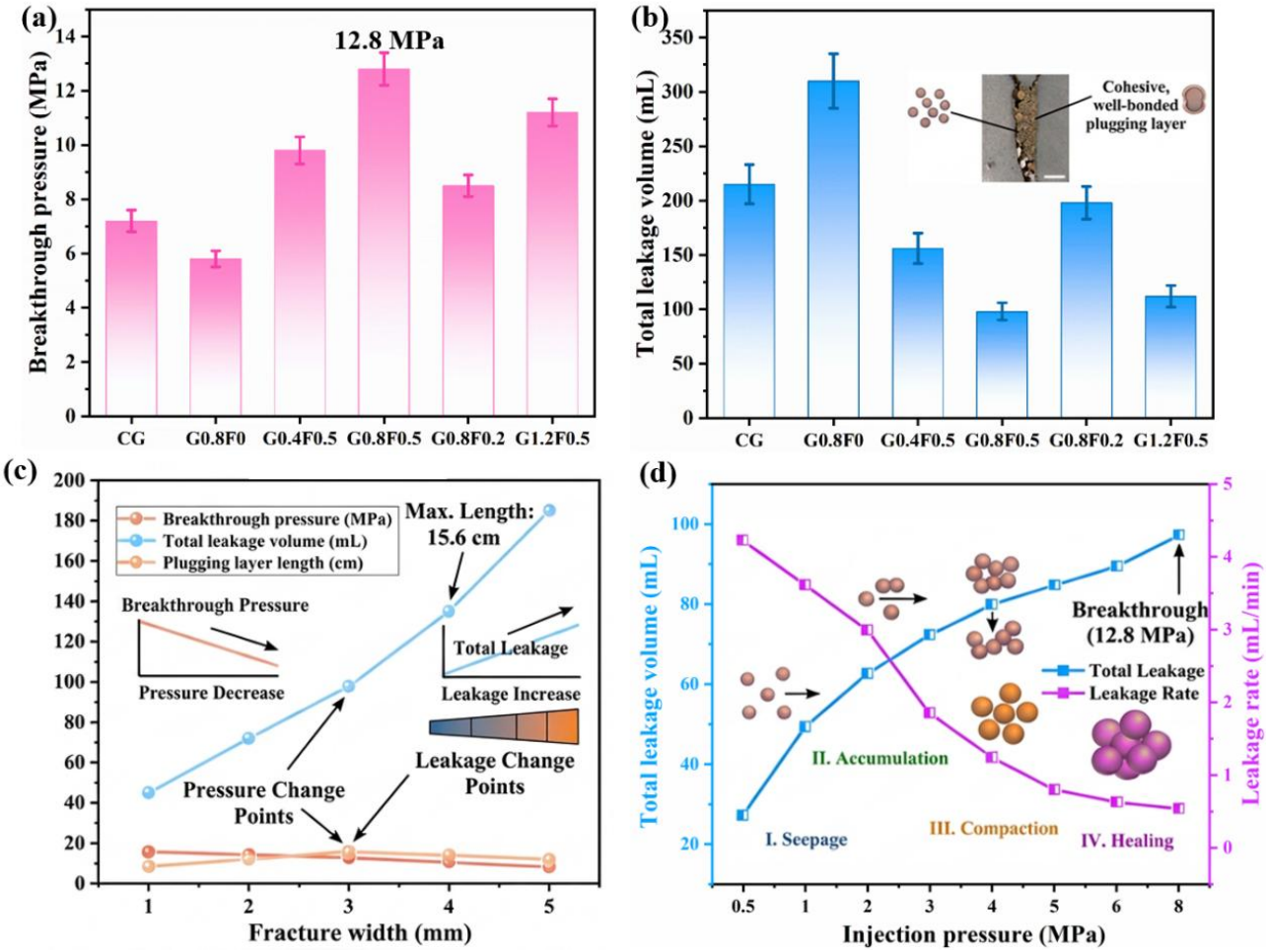


**Figure 7.** Dynamic fracture plugging performance. (**a**) Breakthrough pressures. (**b**) Cumulative fluid losses. (**c**) Effect of fracture width. (**d**) Injection pressure and fluid loss rate over time.

The adaptability of G0.8F0.5 to varying geometric constraints was subsequently tested, as illustrated in Figure 7c. An increase in the fracture width from 1 mm to 5 mm triggered a steady decrease in the breakthrough pressure, dropping from 15.6 MPa down to 8.2 MPa, accompanied by a fluid loss increase from 45 mL to 185 mL. Notably, the pressure decline was gradual within the 1–3 mm range but accelerated substantially between 3 and 5 mm. The maximum seal length of 15.6 cm was achieved precisely at the 3 mm width, indicating optimal particle transport and spatial accumulation at this dimension. Figure 7d chronicles the evolutionary sequence of the sealing layer formed by G0.8F0.5 at 3 mm, categorizing it into five chronological phases: (1) Leakage phase from 0.5 to 2.0 MPa, marked by a declining flow rate from 4.2 to 2.8 mL/min and a 62 mL cumulative loss. (2) Accumulation phase traversing 3.0 to 4.0 MPa, where the rate plummeted to 0.8 mL/min. (3) Compaction phase between 5.0 and 6.0 MPa, featuring minimal seepage below 0.3 mL/min. (4) Healing phase spanning 6.0 to 8.0 MPa, characterized by zero flow and a finalized cumulative loss of 98 mL. (5) Breakthrough phase at 12.8 MPa, marked by catastrophic seal failure and resumed effluent flow.

### 3.6. Drilling Hydraulics Simulation and ROP Enhancement

The Herschel–Bulkley rheological constants derived for all formulations are tabulated in Table 5. The optimized G0.8F0.5 exhibited a yield stress $\tau_0$ of 1.9 Pa, along with a consistency coefficient K evaluated at 0.31 Pa·s$^n$. The flow behavior index n was calculated as 0.52 ($R^2$ = 0.996). Relative to the CG baseline, G0.8F0.5 possesses significantly reduced yield stress and consistency values alongside a lower flow index, endowing it with superior shear-thinning characteristics particularly within high-shear regimes.

**Table 5.** Herschel–Bulkley model fitting parameters for the tested fluids.

| Sample | $\tau_0$ (Pa) | $K$ (Pa·s$^n$) | n | $R^2$ |
|---|---|---|---|---|
| CG | 5.2 | 0.85 | 0.65 | 0.998 |
| G0.8F0 | 2.8 | 0.42 | 0.58 | 0.995 |
| G0.4F0.5 | 2.1 | 0.36 | 0.54 | 0.996 |
| G0.8F0.5 | 1.9 | 0.31 | 0.52 | 0.996 |
| G0.8F0.2 | 2.2 | 0.38 | 0.55 | 0.995 |
| G1.2F0.5 | 2.5 | 0.45 | 0.56 | 0.994 |

Hydraulic simulations visualized in Figure 8a confirm that replacing CG with G0.8F0.5 reduces the annular pressure drop by 20.5% down to 6.2 MPa while amplifying the bit hydraulic horsepower by 21.1% up to 155 kW. This dual benefit—reduced pumping pressure constraints coupled with enhanced rock-breaking energetics—synergistically accelerates drilling operations. Consequently, as shown in Figure 8b, G0.8F0.5 achieved a low ECD of 1.67 g/cm$^3$, undershooting the 1.73 g/cm$^3$ of CG, while boosting the relative rate of penetration (ROP) by 26%. Such ECD reduction is crucial for safely navigating formations featuring narrow pressure margins, as it permits operators to employ denser muds or higher flow rates without inducing hydraulic fracturing. Although the uncoordinated G0.8F0 also exhibited favorable hydraulics, its proven inability to seal fractures disqualifies it as a viable while-drilling LCM. Conversely, the heavily modified G1.2F0.5 generated an elevated annular pressure drop of 7.0 MPa and an ECD of 1.70 g/cm$^3$, indicating that excessive SMA content introduces prohibitive pumping resistance that partially negates the advantages of shear-thinning. Parametric sensitivity analysis for G0.8F0.5 across varying pump rates, plotted in Figure 8c, revealed that accelerating the flow from 30 L/s to 35 L/s elevates the ECD to 1.73 g/cm$^3$, a value mirroring that of CG operating merely at 30 L/s. Thus, implementing G0.8F0.5 safely accommodates a flow rate increase up to

approximately 33 L/s without exceeding baseline ECD limits, offering a direct pathway to further ROP enhancement.

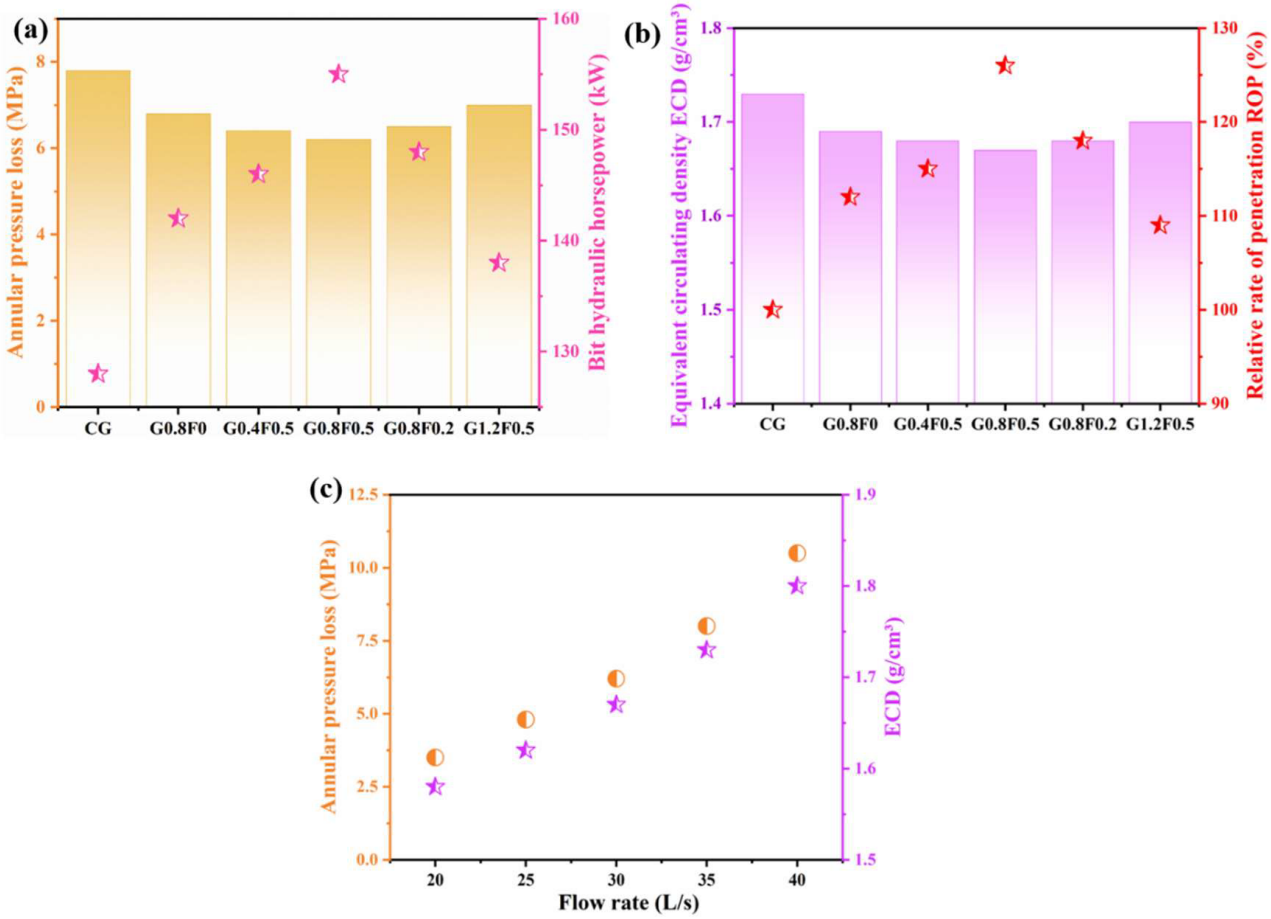


**Figure 8.** Drilling hydraulics simulations. (**a**) Annular pressure drop vs. bit hydraulic horsepower. (**b**) ECD vs. relative ROP. (**c**) Effect of pump rate on ECD.

It must be emphasized that the 26% ROP enhancement derived from the empirical correlation is strictly a simulation-based estimate under idealized hydraulic conditions. In practical field operations, the actual ROP is a complex response governed by a multi-factorial matrix including bit type, weight on bit (WOB), rotary speed (RPM), lithology, hole cleaning efficiency, differential pressure, and formation rock mechanics. Therefore, the simulated data presented herein serve solely to demonstrate the hydraulic potential of the shear-responsive fluid in optimizing annular pressure limits, rather than representing a demonstrated field result.

### *3.7. Comprehensive Plugging Mechanism*

Synthesizing the rheological, physical, and hydraulic data, the plugging mechanism of G0.8F0.5 within natural fractures operates through four orchestrated stages: shear-thickening guided migration, particulate accumulation and compaction, ionically triggered self-healing, and dual-network reinforcement. This conceptual framework is illustrated in Figure 9.

During the initial pumping phase inside the drill string, the fluid is subjected to extreme shear rates exceeding 100 $s^{-1}$, which collapses the dynamic network to maintain a highly pumpable viscosity of just 245 mPa·s. Upon penetrating the fracture aperture, the cross-sectional geometry drops the localized shear rate to a 10–20 $s^{-1}$ window. Crucially, this range perfectly intercepts the gel's critical shear threshold of 14.2 $s^{-1}$, instantly trigger-

ing shear-induced hydrophobic association. The resulting viscosity surge to 6180 mPa·s acts as a hydrodynamic brake, retarding particle migration and forcing them to accumulate strategically deep within the fracture at the 12–18 cm mark. By comparison, formulations with mismatched critical thresholds either over-penetrated without accumulating due to delayed thickening, as seen with G0.4F0.5, or bridged prematurely at the very entrance, as observed for G1.2F0.5.

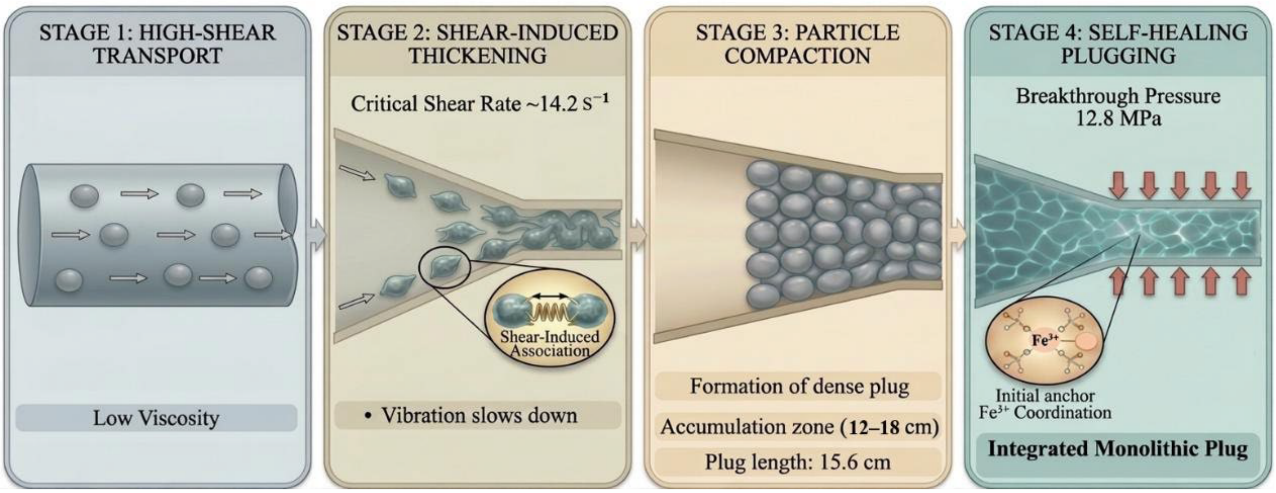


**Figure 9.** Schematic illustration depicting the sequential fracture plugging mechanism of G0.8F0.5.

Once the physical particulate slug is deposited, the thermal environment at 80 °C activates the inter-particle self-healing process. Free $Fe^{3+}$ ions and uncoordinated sulfonic groups located at the fractured interfaces rapidly form new ionic bridges, generating initial adhesion that anchors adjacent particles together. Over a subsequent 6–12 h window, thermally driven macromolecular diffusion facilitates the reconstruction of interfacial hydrophobic domains, while the dynamic breaking and reforming of ionic bonds homogenizes the crosslink distribution [27,30]. This transforms the granular pack into a monolithic, continuous gel phase. Tensile recovery data, which confirmed a 94.9% strength restoration for G0.8F0.5 in stark contrast to the zero recovery of the $Fe^{3+}$-free variant, underscores that ionic coordination is the absolute prerequisite for cementing the plugging layer [17,31–33].

Following complete self-healing, the robust interpenetrating dual-network architecture grants the unified gel plug exceptional mechanical resilience. Exhibiting a tensile strength of 1425 kPa, it conforms seamlessly to the fracture walls and successfully withstands extrusion pressures up to 12.8 MPa. However, enlarging the fracture width beyond 4 mm disproportionately diminishes the inlet shear rate, muting the shear-thickening effect and thereby lowering the breakthrough pressure below 10.5 MPa. Ultimately, the unparalleled performance of G0.8F0.5 is rooted in its meticulously engineered triad of properties: a critical shear rate perfectly synchronized with fracture entry dynamics, a moderate thickening magnitude promoting deep compaction, and an optimized 0.5 wt% $Fe^{3+}$ concentration ensuring maximal interfacial healing without stifling chain mobility.

## 4. Conclusions

In this study, a shear-responsive gel designed for lost circulation mitigation was synthesized utilizing a dual physical crosslinking strategy governed by hydrophobic association and ionic coordination. The influences of hydrophobic monomer and $Fe^{3+}$ concentrations on the shear rheology, self-healing capabilities, and fracture sealing efficiencies were systematically evaluated, successfully bridging the fundamental critical shear rate with practical drilling hydraulics. Empirical results demonstrated that modulating the hydrophobic

monomer content enables the continuous tuning of the critical shear rate between 8.6 and 22.5 $s^{-1}$. Notably, the optimized formulation designated as G0.8F0.5 exhibited a critical shear rate of 14.2 $s^{-1}$, which seamlessly aligns with the typical shear rate window of 10 to 20 $s^{-1}$ encountered at fracture inlets. This specific composition maintained a highly pumpable viscosity of 245 mPa·s under high-shear conditions inside the drill string, but underwent dramatic shear-induced thickening to 6180 mPa·s upon entering the fracture, thereby successfully reconciling the otherwise conflicting requirements of low pumping resistance and robust in situ retention. Furthermore, the formation of ionic coordination bonds between $Fe^{3+}$ and sulfonic acid groups was identified as the pivotal mechanism driving self-healing. Following 12 h thermal conditioning at 80 °C, G0.8F0.5 achieved an impressive tensile strength recovery of 94.9%, a regenerative capability that was entirely absent in the uncoordinated baseline. Dynamic plugging evaluations using a 3 mm tapered fracture model confirmed that G0.8F0.5 could withstand a robust breakthrough pressure of 12.8 MPa while restricting cumulative fluid loss to a mere 98 mL. The resulting seal consolidated deeply within the distal section of the fracture as a monolithic gel plug, comprehensively outperforming conventional polyacrylamide alternatives. Finally, drilling hydraulic simulations revealed that deploying this advanced gel could reduce the equivalent circulating density (ECD) by 0.06 $g/cm^3$ and boost the rate of penetration (ROP) by approximately 26%, effectively minimizing the non-productive time typically associated with lost circulation events. By achieving an optimal equilibrium among critical shear rate, shear-thickening amplitude, and healing efficiency, G0.8F0.5 emerges as a superior, quantitatively designable material paradigm for concurrent drilling and lost circulation control.

**Author Contributions:** S.H., Investigation, Writing—original draft; Z.Z., Conceptualization, Methodology; J.M., Writing—original draft; B.L., Writing—review and editing; R.Y., Data curation; Z.J., Formal analysis; S.L., Writing—review and editing. All authors have read and agreed to the published version of the manuscript.

**Funding:** This research received no external funding.

**Data Availability Statement:** The original contributions presented in this study are included in the article. Further inquiries can be directed to the corresponding author.

**Conflicts of Interest:** Shoushuai Huang, Zhigang Zhang, Jian Mao, Bin Li, Ruigang Yuan and Zhaomin Jiang were employed by the Directional Well Technical Service Company of XDEC. The remaining author declares that the research was conducted in the absence of any commercial or financial relationships that could be construed as potential conflicts of interest.

## References

1. Kang, Y.; Ma, C.; Xu, C.; You, L.; You, Z. Prediction of Drilling Fluid Lost-Circulation Zone Based on Deep Learning. *Energy* **2023**, *276*, 127495. [CrossRef]
2. Kong, X.; Chen, M.; Zhang, C.; Liu, Z.; Jin, Y.; Wang, X.; Liu, M.; Li, S. Optimization of High Temperature-Resistant Modified Starch Polyamine Anti-Collapse Water-Based Drilling Fluid System for Deep Shale Reservoir. *Molecules* **2022**, *27*, 8936. [CrossRef] [PubMed]
3. Qiu, J.; Bai, Y.; Sun, J.; Dai, L.; Lei, S.; Liu, F. Experimental Study on an Oil-Based Polymer Gel for Lost Circulation Control in High-Temperature Fractured Formation. *J. Appl. Polym. Sci.* **2022**, *139*, 51763. [CrossRef]
4. Xu, H.; Zhu, Y.; Liu, Y.; Fan, W.; Tang, L.; Chen, T.; Wang, Y.; Yang, F. Temperature-Sensitive Polymer Grafted with Nano-$SiO_2$ Improves Sealing and Inhibition Performance of Shale Water-Based Drilling Fluid. *Colloids Surf. A* **2024**, *698*, 134531. [CrossRef]
5. Sun, D.; Yang, Y.; Ma, W.; Ye, S.; Zhang, H.; Zhang, J.; Yang, B. Heat-Resistant Hydrogel for Temporary Plugging in High-Temperature and High-Pressure Fractured Reservoirs. *ACS Appl. Polym. Mater.* **2023**, *5*, 7746–7754. [CrossRef]
6. Cao, Z.; Miao, C.; Du, F.; Zhu, D.; Teng, T.; Xue, Y. A Bifurcation Dynamical Analysis of a Non-Darcy Seepage System in Post-Failure Rock Based on a Novel Truncated Spectral Method. *Processes* **2026**, *14*, 1468. [CrossRef]

7. Hou, Y.; Miao, C.; Zhu, D.; Li, Z.; Du, F.; Wang, W.; Yang, X.; Cao, Z. Flow Mechanism of Grouting Slurry in Rough Fracture Based on CFD-DEM Coupling Method. *Processes* **2026**, *14*, 1307. [CrossRef]
8. Xu, C.; Zhang, H.; Kang, Y.; Zhang, J.; Bai, Y.; Zhang, J.; You, Z. Physical Plugging of Lost Circulation Fractures at Microscopic Level. *Fuel* **2022**, *317*, 123477. [CrossRef]
9. Sun, J.; Bai, Y.; Cheng, R.; Lyu, K.; Liu, F.; Feng, J.; Lei, S.; Zhang, J.; Hao, H. Research Progress and Prospect of Plugging Technologies for Fractured Formation with Severe Lost Circulation. *Pet. Explor. Dev.* **2021**, *48*, 732–743. [CrossRef]
10. Guo, C.; Jiang, G.; Guan, J.; Huang, S.; Guo, Y.; He, Y.; Yang, L.; Dong, T. Preparation and Performance Evaluation of a Thixotropic Polymer Gel for Loss Circulation Control. *Fuel* **2024**, *371*, 132148. [CrossRef]
11. Sun, D.; Yang, Y.; Liu, Y.; Wu, Z.; Zhang, H. Strengthening the Hydrogel for Lost Circulation Control through In Situ Self-Assembled Nanocomposite Networks. *Energy Fuels* **2023**, *37*, 4321–4330. [CrossRef]
12. Cui, X.; Wang, C.; Huang, W.; Zhang, S.; Chen, H.; Wu, B.; Qin, D.; Zheng, X. Multiple Hydrogen Bonding-Assisted High-Strength Hydrogel of Silica/Polyacrylamide Nanocomposite Cross-Linked with Polyethylenimine. *ACS Omega* **2023**, *8*, 39401–39407. [CrossRef] [PubMed]
13. Zhu, L.; Cui, C.; Jing, T.; Tan, S.; Liu, X.; Yu, M. Strong and broadband microwave absorption under thin thickness induced by multiple dielectric relaxation and multiple magnetic resonances through the dual nanocrystalline phases in amorphous FeSiBCr flakes. *Acta Phys.-Chim. Sin.* **2026**, *42*, 100331. [CrossRef]
14. Azimi Dijvejin, Z.; Ghaffarkhah, A.; Sadeghnejad, S.; Vafaie Sefti, M. Effect of Silica Nanoparticle Size on the Mechanical Strength and Wellbore Plugging Performance of SPAM/Chromium (III) Acetate Nanocomposite Gels. *Polym. J.* **2019**, *51*, 693–707. [CrossRef]
15. Zhao, Z.; Sun, J.; Liu, F.; Bai, Y.; Wang, R. A Laboratory Study of Self-Healing Hydrophobic Association Gels Used as Lost Circulation Material. *Colloids Surf. A* **2022**, *646*, 128964. [CrossRef]
16. Xu, P.; Yu, J.; Xie, L. Synthesis and Evaluation of Plugging Gel Resistant to 140 °C for Lost Circulation Control: Effective Reduction in Leakage Rate in Drilling Process. *Polymers* **2024**, *16*, 1658. [CrossRef] [PubMed]
17. Liu, Y.; Ren, Y.; Dong, H.; Chen, C.; Liu, X.; Lei, Y.; Xiao, X.; Wang, L. High-Strength Thermally Activated Shape-Adaptive Plugging Hydrogels with Plastic Semicrystalline Metallosupramolecular Polymer Networks. *ACS Appl. Polym. Mater.* **2024**, *6*, 10478–10487. [CrossRef]
18. Wang, C.; Sun, J.; Long, Y.; Wang, R.; Qu, Y.; Peng, L.; Ren, H.; Gao, S. A Re-Crosslinkable Composite Gel Based on Curdlan for Lost Circulation Control. *J. Mol. Liq.* **2023**, *371*, 121010. [CrossRef]
19. Wang, K.; Guo, Y.; Wen, J.; Yang, H.; Zhang, H. Magnetic Smart Polymer Gel with Directional Plugging for Conformance Control in Oil Reservoirs. *J. Mol. Liq.* **2024**, *405*, 125046. [CrossRef]
20. Fang, J.; Zhang, X.; Li, L.; Zhang, J.; Shi, X.; Hu, G. Research Progress of High-Temperature Resistant Functional Gel Materials and Their Application in Oil and Gas Drilling. *Gels* **2022**, *9*, 34. [CrossRef] [PubMed]
21. Bai, Y.-R.; Dai, L.-Y.; Sun, J.-S.; Jiang, G.-C.; Lv, K.-H.; Cheng, R.-C.; Shang, X.-S. Plugging Performance and Mechanism of an Oil-Absorbing Gel for Lost Circulation Control While Drilling in Fractured Formations. *Pet. Sci.* **2022**, *19*, 2941–2958. [CrossRef]
22. Shamlooh, M.; Hamza, A.; Hussein, I.A.; Nasser, M.S.; Magzoub, M.; Salehi, S. Investigation of the Rheological Properties of Nanosilica-Reinforced Polyacrylamide/Polyethyleneimine Gels for Wellbore Strengthening at High Reservoir Temperatures. *Energy Fuels* **2019**, *33*, 6829–6836. [CrossRef]
23. Nazemi, R.; Moghadasi, J.; Ashoori, S. Design and Experimental Study on Rheological Behavior and Sealing Performance of Shear Sensitive Fluids to Control Lost Circulation during Drilling. *Geoenergy Sci. Eng.* **2024**, *237*, 212830. [CrossRef]
24. Al Dushaishi, M.F.; Nygaard, R.; Stutts, D.S. Effect of Drilling Fluid Hydraulics on Drill Stem Vibrations. *J. Nat. Gas. Sci. Eng.* **2016**, *35*, 1059–1069. [CrossRef]
25. Geng, Y.; Lin, X.Y.; Pan, P.; Shan, G.; Bao, Y.; Song, Y.; Wu, Z.L.; Zheng, Q. Hydrophobic Association Mediated Physical Hydrogels with High Strength and Healing Ability. *Polymer* **2016**, *100*, 61–68. [CrossRef]
26. Ferrás, L.L.; Nóbrega, J.M.; Pinho, F.T. Analytical Solutions for Newtonian and Inelastic Non-Newtonian Flows with Wall Slip. *J. Non-Newton. Fluid Mech.* **2012**, *175–176*, 76–88. [CrossRef]
27. Liu, Y.; Zhou, L.; Wan, X.; Tang, Y.; Liu, Q.; Li, W.; Liao, J. Synthesis and characterization of a temperature-sensitive microcapsule gelling agent for high-temperature acid release. *ACS Omega* **2024**, *9*, 20849–20858. [CrossRef] [PubMed]
28. Liu, Y.; Li, W.; Xiao, Z.; Ji, S.; Liu, Q.; Tang, Y.; Zhang, Y.; Wang, J. Recent Progress in Organic Inhibitors for Anticorrosion in Complex Acid Environments. *Coatings* **2026**, *16*, 150. [CrossRef]
29. Li, G.; Yang, H.; Liu, F.; Zhou, J.; Wu, C.; Zeng, H.; Yao, C.; Zhang, C.; Kang, Y.; Wang, J. Highly Stretchable Hydrogel Membranes with Metal-Ion Coordination for Scalable Stable Osmotic Energy Conversion. *Adv. Funct. Mater.* **2026**, *36*, e15774. [CrossRef]
30. Xue, Z.; Hu, M.; Miao, X.; Zang, L.; Guo, J. Synthesis of a Hydrophobic Associating Polymer and Its Application in Plugging Spacer Fluid. *RSC Adv.* **2022**, *12*, 11402–11412. [CrossRef] [PubMed]
31. Deng, Z.; Zhou, W.; Yue, H.; Deng, H.; Zhang, H.; Zheng, Y.; Fu, H. Analysis of Hydration Process of Smelter Slag Plugging Fluid Activated with Alkalis. *Constr. Build. Mater.* **2021**, *269*, 121281. [CrossRef]

32. Al-Majali, M.R.; Zhang, M.; Al-Majali, Y.T.; Trembly, J.P. Impact of raw material on thermo-physical properties of carbon foam. *Can. J. Chem. Eng.* **2025**, *103*, 1309–1318. [CrossRef]
33. Zhao, J.; Zhang, M.; Wang, C.; Yu, W.; Zhu, Y.; Zhu, P. First-principles study of CO, $NH_3$, HCN, CNCl, and $Cl_2$ gas adsorption behaviors of metal and cyclic C–metal B-and N-site-doped h-BNs. *Electron. Mater. Lett.* **2025**, *21*, 268–288. [CrossRef]